Title
Many-isocenter optimization for robotic radiotherapy

Journal
Physics in Medicine and Biology, 65(4)

ISSN
0031-9155

Authors
Lyu, Qihui
Neph, Ryan
Yu, Victoria Y
et al.

Publication Date
2020-02-01

DOI
10.1088/1361-6560/ab63b8

Peer reviewed

HHS Public Access

Author manuscript

Phys Med Biol. Author manuscript; available in PMC 2021 February 10.

Published in final edited form as:

Phys Med Biol. ; 65(4): 045003. doi:10.1088/1361-6560/ab63b8.

Many-isocenter Optimization for Robotic Radiotherapy

Qihui Lyu[1], **Ryan Neph**[1], **Victoria Y Yu**[1], **Dan Ruan**[1], **Salime Boucher**[2], **Ke Sheng**[1]

[1]Department of Radiation Oncology, University of California Los Angeles, Los Angeles, CA, 90095, USA

[2]RadiaBeam Technologies, Santa Monica, CA 90404

Abstract

Despite significant dosimetric gains, clinical implementation of the 4π non-coplanar radiotherapy on the widely available C-arm gantry system is hindered by limited clearance, and the need to perform complex coordinated gantry and couch motion. A robotic radiotherapy platform would be conducive to such treatment but a new conflict between field size and MLC modulation resolution needs to be managed for versatile applications. This study investigates the dosimetry and delivery efficiency of purposefully creating many isocenters to achieve simultaneously high MLC modulation resolution and large tumor coverage. An integrated optimization framework was proposed for simultaneous beam orientation optimization (BOO), isocenter selection, and fluence map optimization (FMO). The framework includes a least-square dose fidelity objective, a total variation term for regularizing the fluence smoothness, and a group sparsity term for beam selection. A minimal number of isocenters were identified for efficient target coverage. Colliding beams excluded, high-resolution small-field 4π intensity-modulated radiotherapy (IMRT) treatment plans with 50cm source-to-isocenter distance (SID-50) on 10 Head and Neck (H&N) cancer patients were compared with low-resolution large-field plans with 100cm SID (SID-100). With the same or better target coverage, the average reduction of [Dmean,Dmax] of 20-beam SID-50 plans from 20-beam SID-100 plans were [2.09 Gy,1.19 Gy] for organs at risk (OARs) overall, [3.05 Gy,0.04 Gy] for parotid gland, [3.62 Gy,5.19 Gy] for larynx, and [3.27 Gy,1.10 Gy] for mandible. R50 and integral dose were reduced by 5.3% and 9.6% respectively. Wilcoxon signedrank test showed significant difference ($p<0.05$) in planning target volume (PTV) homogeneity, PTV Dmax, R50, Integral dose, and OAR Dmean and Dmax. The estimated delivery time of 20-beam [SID-50, SID-100] plans were [19,18] minutes and [14,9] minutes, assuming 5 fractions and 30 fractions, respectively. With clinically acceptable delivery efficiency, many-isocenter optimization is dosimetrically desirable for treating large targets with high modulation resolution on the robotic platform.

1. Introduction

Since its initial introduction in 1982 (Brahme *et al* 1982), intensity-modulated radiotherapy (IMRT) has been compared favorably to the 3-dimensional (3D) conformal radiation therapy due to enhanced target coverage and improved organs at risk (OAR) sparing. Subsequently,

Disclosure of Conflicts

Dr. Ke Sheng is a co-founder of Celestial Oncology.

the technologies involving inverse treatment optimization and multileaf collimators (MLC) for intensity modulation have been rapidly developed and adopted in the clinic. More recent technological advances such as helical tomotherapy and volumetric modulated arc therapy (VMAT) further streamlined IMRT delivery while maintaining comparable plan quality (Rao *et al* 2010, Teoh *et al* 2011, Vanetti *et al* 2009). Since further plan quality improvement is hampered by the limited beam geometry in the coplanar IMRT and VMAT mode, planning methods using optimized non-coplanar beam angles, termed 4π radiation therapy (Dong *et al* 2013a, 2013b, Smyth *et al* 2019a, Meedt *et al* 2003, Laing *et al* 1993, Chapet *et al* 2006, Smyth *et al* 2013, Murzin *et al* 2018, Dong *et al* 2014b, Pugachev *et al* 2001, Voet *et al* 2012, Krayenbuehl *et al* 2006) have been developed. Compared with state-of-the-art coplanar IMRT methods, 4π significantly reduced high dose spillage to the normal tissue. The improved dose compactness is desirable for stereotactic radiotherapy where the normal tissue toxicities are manifested in the high dose region (Yang *et al* 2010).

Despite the demonstrated dosimetric benefits, 4π radiotherapy clinical adoption is not straightforward. Studies have shown the feasibility of delivering 4π IMRT (Yu *et al* 2018) and 4π VMAT (Smyth *et al* 2019b, Wilson *et al* 2017) plans on the C-arm gantry platform, where the non-coplanar beam orientations require the combination of couch and gantry rotation to achieve. However, the combined motion increases treatment delivery time, risk of collision and unwanted patient secondary motion. Couch rotations also create challenges to maintain constant monitoring of the patient position. The more complex dry run and QA before treatment delivery is yet another obstacle.

Alternatively, a robotic linac platform is more conducive for the non-coplanar and non-isocentric treatment. For instance, the CyberKnife Robotic Radiosurgery System (Accuray, Sunnyvale, CA, USA) mounts a 6-MV linac to an articulated robotic arm that allows both non-coplanar and non-isocentric treatments without moving the patient. Currently, CyberKnife does not have access to all non-coplanar angles (Pollom *et al* 2019) but this engineering challenge may be overcome with a more compact linac design, modification to the robotic arm or the treatment room. Celestial Oncology (Santa Monica, CA, USA) is currently developing a more compact linac with the complete access to the 4π Steradian angles around the patient. However, to make the linac head smaller for the robotic platform, a more stringent requirement is placed on the MLC form factor. Both the number and the travel of the leaves are limited for the compact linac head size, creating a significant challenge in attaining both large field-of-view (FOV) and high modulation resolution. A method to achieve both goals would significantly increase the versatility of robotic linacs.

Thus far, 4π radiotherapy is mainly performed with the assumption of isocentric geometry and 100 cm source-to-isocenter distance (SID) (Yu *et al* 2018, Dong *et al* 2014a), which is the native geometry of the ubiquitous C-arm gantry linacs with one degree of rotational freedom during treatment. Multiple isocenter treatment on a conventional C-arm linac is cumbersome and potentially hazardous due to the increased chance of geometric error and collision. It has been performed for large targets when the isocentric geometry cannot provide a sufficiently large FOV to cover the entire target, such as breast (Kim *et al* 2019, Amoush *et al* 2015), supraclavicular fossa (Amoush *et al* 2015), craniospinal radiotherapy (Wang *et al* 2013), and etc (Hong *et al* 2002, Zeng *et al* 2007).

From robotic linacs, varying the SID and adding the number and locations of isocenters as a new degree of freedom appears to be a logical extension of the 4π research due to the following considerations. 1. Using a smaller SID would allow a higher MLC modulation resolution that is dosimetrically beneficial in highly complex cases. 2. Using a smaller SID results in more rapid dose fall-off in the beam direction due to the more prominent inverse square effect. 3. The small single FOV can be compensated by using more than one isocenters to cover the entire tumor. 4. The treatment efficiency of using more isocenters is compensated by the increase in the dose rate at the shorter distance. On the other hand, most beam angles with substantially shorter distances, i.e., 50cm SID, are geometrically prohibited on the C-arm gantry.

In this study, we strategically divide a large target into many smaller targets each with its own isocenter, to achieve small FOV beam high-resolution delivery at a shorter distance. A many-isocenter planning problem was solved to simultaneously optimize the beams and fluence maps. In this study, to determine the dosimetric benefit of many-isocenter planning, we adopt the geometry of the new robotic linac that is currently under development at Celestial Oncology. However, methods used in this study are generalizable to any radiation delivery platforms that have access to large non-coplanar angles, non-isocentric beams, and substantially different source-to-tumor distances.

2. Materials and methods

2.1. Robotic platform model

Figure 1(A) shows the robotic radiotherapy platform under development by Celestial Oncology, which reduced the linac head size by using a compact x-band 6MV source and reducing the distance between the X-ray source and the MLC. To study the dosimetry and delivery efficiency, the two SIDs are considered: 100 cm and 50 cm. At SID-100, the projected MLC leaf width is 1 cm, and the FOV is 20cm by 20cm with a total of 20 leaves per bank. The physical size and the number of the leaves were determined based on the fabrication practicality and size of the robotic linac head. At SID-50, the projected MLC leaf width is 0.5cm, and the FOV is 10cm by 10cm. For Head and Neck (H&N) cancer with the planning target volume (PTV) up to 20 cm, the target can be fully covered by a SID-100 beam (Figure 1(B)). For SID-50, beams of many isocenters are required to efficiently cover the entire target (Figure 1(C)).

2.2. Determine isocenter locations

We use the following method to determine the position of isocenters when the FOV is not large enough to cover the entire target. Figure 2 shows an illustration of the PTV, bounding box, and isocenters. The bounding box of a target is defined as the smallest cuboid that fully covers the entire PTV in the scanner coordinate system. The dimension of the bounding box is denoted by $[B_x, B_y, B_z]$, and the beam FOV is denoted by $[F_x, F_y, F_z]$. We first divide the bounding box to N_x, N_y, N_z number of identically sized boxes in the x, y, z directions respectively, where $N_w = \lceil B_w/F_w \rceil$, $w = \{x, y, z\}$. ($\lceil \cdot \rceil$ represents the ceiling operation). For each divided box, the isocenter position is set at the center of mass (CoM) of the partial PTV within the box. The rationale behind the method is that each isocenter will be 'in charge' of

a partial PTV for which the x, y, and z dimensions are smaller than the nominal beam FOV. Note that this method locates a set of isocenters that are adequate to cover the entire PTV, but it does not necessarily demand all identified isocenters to be used in the final plan. The BOO algorithm, which is discussed in the next section, determines whether the candidate beams and the isocenters are utilized in the final plan.

2.3. Integrated Fluence Map Optimization, Beam Orientation Optimization, and isocenter selection.

The integrated framework for fluence map optimization (FMO), beam orientation optimization (BOO), and isocenter selection is formulated as

$$\begin{aligned} &\underset{x}{\text{minimize}} \ \frac{1}{2}\|W(Ax-d)\|_2^2+\lambda\|Dx\|_1+\gamma\sum_{b,i}W_{b,i}\|x_{b,i}\|_2^{\frac{1}{2}} \\ &\text{subject to} \qquad\qquad x\geq 0, \end{aligned} \tag{1}$$

where x is the vectorized fluence map, A is the fluence to dose transformation matrix, d is the vectorized ideal dose distribution, with prescription dose at the PTV and 0 elsewhere. W is the diagonal structure weighting matrix. The matrix D is the derivative matrix, and λ is the corresponding weighting coefficient. $x_{b,i}$ is the vectorized fluence map of beam b and isocenter i, and $w_{b,i}$ is the beam weighting coefficient.

In this formulation, the data fidelity term attempts to find the optimal fluence map $\hat{x}$ such that the calculated dose is as close as possible to the ideal dose. The priorities for the structures of interest are controlled by the diagonal weighting matrix W. The second term is the total variation (TV) regularization which encourages piecewise continuity of the fluence map (Zhu *et al* 2008). The amount of smoothness is controlled by λ.

The third term is the group sparsity term in the form of $l_{2,1/2}$ norm penalty, which encourages most candidate beams to be inactive. The individual beam weights w_b serve as a normalization to correct for the intrinsic norm differences among candidate beams, which has been widely used in compressed sensing (Blumensath and Davies 2010). The individual beam weights are calculated by $w_{b,i}=\left(\frac{\text{mean}\left(A_{PTV}^{b,i}\vec{1}\right)}{\sqrt{n_{b,i}}}\right)^{1/2}$, where $n_{b,i}$ is the number of beamlets in beam b for isocenter i, and $A_{PTV}^{b,i}$ is the fluence to dose transformation matrix within the PTV, for beam b directed at isocenter i. The parameter γ controls the global sparsity level, which is tuned automatically to achieve the desired number of beams. At every 1000 iterations, the current number of selected beams is checked and compared with the desired number of beams. The value of γ is increased by a factor of 1.5 if there are more beams selected than required, and decreased by a factor of 1.5 if there are not enough beams selected. The optimization problem was solved with the Fast Iterative Shrinkage-Thresholding Algorithm (FISTA) (Beck & Teboulle 2009). To apply FISTA on the optimization problem (1), smooth approximation was made to the total variation term and the problem was formulated in the canonical form of FISTA. Details on the solver can be found in the Appendix A1.

2.4. Evaluation

The efficacy of the optimization algorithm was tested on 10 consecutive H&N patients who have been diagnosed with oropharyngeal cancer. The patients were CT-simed with immobilization mask. The contours and prescription follow 2018 American Society of Therapeutic Radiation Oncology (ASTRO) head and neck treatment guideline.

Table 1 summarizes the PTV volumes, PTV bounding box dimensions, number of isocenters, number of sampled beams, and number of candidate beams (non-colliding beams) for all patients. For cases with fewer than or equal to four isocenters, for each isocenter, 1162 beams were uniformly sampled in the 4π space with 6° of separation. For cases with more than 4 isocenters, to reduce the computation cost of both dose calculation and optimization, for each isocenter 290 beams were uniformly sampled with 12° of separation, and the angular sampling of adjacent isocenters differ by 6° to compensate the coarse sampling. For example, if the angular sampling of one isocenter is {0°, 12°, 24°, … }, then the angular sampling of the adjacent isocenter is {6°, 18°, 30°, … }. A computer-aided-design (CAD) model of a robotic arm platform and a 3D optically reconstructed surface of a human subject were utilized to determine the patient-specific collision-free space (Yu *et al* 2015). After excluding the colliding beams, the number of candidate-beams for each case can be found in Table 1.

The beamlet dose calculation used a convolution/superposition code with a 6 MV x-ray polyenergetic kernel, as described in our previous publication (Neph *et al* 2019). The beamlet resolution at the isocenter was 0.5×0.5 cm^2 for SID at 50 cm and 1×1 cm^2 for SID at 100 cm, adjusting for the beam divergence effect. The dose array resolution was $0.25\times0.25\times0.25$ cm^3. As a sensitivity analysis, we compared the SID-50 plan quality against the SID-100 with the number of selected beams ranging from 15 to 50, based on the corresponding data fidelity values. The plans with 20 beams were used for further evaluation on plan efficiency and plan quality. The delivery time was estimated for both a hypofractionation scenario (assuming 5 fractions), and a conventional fractionation scenario (assuming 30 fractions), for all 20-beam plans. The estimation includes the times for MLC leaf travel, x-ray delivery, and Linac head travel. To estimate the MLC leaf travel time, the fluence map was first stratified into a finite number of discrete levels, and then sequenced using a reducing level method (Xia and Verhey 1998). Each sequenced segment was further divided into a few deliverable segments, and all segments within one beam were reordered to reduce MLC leaf motion by solving a travelling salesman problem (TSP) (Reinelt 1991). The same algorithm was used to reorder the beams and minimize the amount of Linac head travel. Note that the stratification was performed only for evaluating delivery efficiency, and all dosimetric evaluations were based on the theoretical dose from optimization. The effects of stratification on the dosimetry are minimal, as demonstrated by the DVH comparison of the plans before and after the sequencing step for patient #1, presented in the supplementary materials.

In the efficiency estimation, the following assumptions on the mechanical specifications were used:

1. The MLC travel speed is at 2.5cm/s at 100cm from the source, and 1.25cm/s at 50cm.
2. The Linac head rotation speed is 1 rpm with respect to the isocenter according to the International Electrotechnical Commission (IEC) safety standard.
3. The effective dose rate is 500MU/min[1] at 100cm from the source accounting for small field output factor and flattening-filter-free dose heterogeneity, and 2000MU/min at 50cm from the source.

PTV statistics including PTV D95, D98, D99, maximum dose (Dmax), and PTV homogeneity (defined as $\frac{D95}{D5}$) were evaluated. Maximum dose is defined as D2 (the dose at 2% of the structure volume), following the ICRU-83 report (Grégoire and Mackie 2011). The dose conformity, R50, and integral dose were also assessed, to quantify the dose conformity, compactness, and total spillage respectively. The dose conformity is defined as the ratio between the patient volume receiving 100% or more of the prescription dose and the PTV volume. The R50 is defined as the 50% isodose volume divided by the target volume. For OAR, the Dmax and mean dose (Dmean) were obtained. Wilcoxon signed rank test was conducted to determine whether a significant difference exists between the SID-50 and the SID-100 for all PTV and OAR statistics.

3. Results

Figure 3 shows the final dose fidelity values of SID-100 and SID-50 plans, varying the number of selected beams between 15 and 50. The average optimization runtime is 25 minutes for 15-beam plans, and 22 minutes for 50-beam plans, on an intel Xeon E5–2670 CPU with 8 physical cores and a base clock speed of 2.6 GHz. For each patient, the dose fidelity values were normalized by the average dose fidelity values of all plans associated with that patient. The plot with error bar shows a summary of all patients. Overall, SID-50 plans resulted in lower dose fidelity value compared with the SID-100 plans using the same number of beams, showing superior plan quality to the SID-100 plans. The gap between SID-50 and SID-100 widens with an increasing number of beams.

Each patient plot is titled with the patient number, the number of isocenters for the SID-50 plan, and the number of isocenters for the SID-100 plan. For example, the first patient plot is entitled: '#1: 4(50), 1(100)', showing that the patient #1 has four isocenters for the SID-50 plan, and one isocenter for the SID-100 plan. For small tumors with only two isocenters (#7, #9) or four isocenters (#1, #8) in the SID-50 plans, SID-50 achieves an unquestionable advantage among all plans. For medium-sized tumors that require 8 isocenters in the SID-50 plans (#2, #4, #5, #6, #10), SID-50 shows clear advantage with 20 or more beams. For the large tumor that requires 12 isocenters (#3) in SID-50 and two isocenters in SID-100, the SID-50 is comparable to SID-100 with fewer than 20 beams but the SID-50 plan is increasingly better with more than 20 beams.

[1]The maximum dose rate of robotic linac is 1000MU/min at 100cm from the source in the flattening filter free mode.

Figure 4 shows the estimated delivery time for all 20-beam plans assuming (A) 5 fractions and (B) 30 fractions for all patients. The delivery time includes three modules: MLC travel time, MU delivery time, and linac head travel time, among which the latter takes the least amount of time, with only around 4s per beam. On average, for a conventional fractionated treatment plan (30 fractions), it takes 14 minutes to deliver a SID-50 plan, and 9 minutes to deliver a SID-100 plan. The longer delivery time of SID-50 is attributed to a longer MLC travel time, which is the most time-consuming module in a 30-fraction treatment. Due to the higher modulation capability of SID-50, the corresponding fluence map is more complicated, requiring more MLC segments in each beam and a longer MLC leaf travel time. For hypofractionation (or Stereotactic Body Radiation Therapy (SBRT)), SID-50 delivery takes 19 minutes, and SID-100 delivery takes 18 minutes. In SBRT, each fraction delivers a greater dose, and the beam-on time is more dominant. The dose rate of SID-50 is four times that of SID-100 due to the inverse square effect. Therefore the 'beam-on' time of SID-50 is substantially shorter. The total delivery time of SID-50 and SID-100 are comparable for SBRT. Video demonstration of the 20-beam SID-50 plan for patient #1 can be found in the supplementary materials.

Figure 5 shows the selected beams in the 20-beam plans of all patients. Note that not all isocenters were utilized in the final plan. For example, for patient #5, the isocenter on the upper, right, and posterior side of the tumor is not utilized. This is partly due to that there are enough beams coming from the left side of the patient, and that the partial PTV of the isocenter has a relatively lower prescription dose. The omission of certain isocenters for efficient delivery is one of the advantages of the integrated optimization framework. Such a decision would be unattainable by a human planner or a greedy algorithm based on only the patient anatomy.

Figure 6 shows the isodose colorwash of SID-100 and SID-50 for two patients (#1 and #2, having 4 and 8 isocenters in the SID-50 plan respectively). Overall, SID-50 achieved a more compact dose distribution. For patient #1, as indicated by the red arrows on the transverse view and coronal view, the SID-50 plan formed a more pronounced dose valley between the two separate PTVs, demonstrating the advantage of higher modulation resolution. In addition, the dose to the spinal cord and mandible was substantially reduced compared with SID-100. For patient #2, the isodose shows reduced low dose spillage in the brain and reduced high dose spillage to the nearby critical organs such as spinal cord and trachea.

Figure 7 shows the DVH comparison of the 20-beam SID-100 plans (solid) and SID-50 plans (dotted) for selected two patients (#1 and #2, having 4 and 8 isocenters in the SID-50 plan respectively). In both cases, SID-50 improved PTV coverage, reduced hot spots within PTV, and reduced mean and max dose for most OARs. For patient #1, the dose to the left parotid, mandible, and spinal cord was substantially reduced in the SID-50 plan. For patient #2, SID-50 markedly improved sparing of the dose-limiting organs, such as the left submandibular gland, right parotid gland, left parotid gland, and trachea. The DVH comparison of the 20-beam plans for all patients can be found in the supplementary materials. To demonstrate the benefits of using non-coplanar beams, we also compared the 4π plans with the coplanar plans for patient #1 and #2. The DVH comparison is presented in the supplementary materials.

Figure 8 shows the PTV statistics, including homogeneity, D99, D98, D95, and D2, for all PTVs (29 PTVs in total). The same PTV in the SID-50 plan (orange) and the SID-100 plan (blue) are connected with lines. Overall, SID-50 achieved comparable PTV D95, D98, D99, improved PTV homogeneity, and reduced hot spot within the target, indicated by the lower D2 (maximum dose) values.

Figure 9 shows the dose conformity, R50, and integral dose of all plans using 20 beams. The dose conformity was comparable between SID-50 and SID-100, but SID-50 reduced R50 by 5.3% and integral dose by 9.6%, indicating a remarkable improvement in dose compactness and overall low dose spillage. Figure 10 Mean and maximum dose for OAR overall and selected critical OARs including parotid gland, larynx, and mandible, for all patients (#1-#10). All plans have 20 beams in total. The SID-100 plan (blue) and the SID-50 plan (orange) of the same patient are connected with lines.

Figure 10 shows the mean and maximum dose for OAR overall and selected critical OARs including parotid gland, larynx, and mandible, for all plans using 20 beams. On average, the SID-50 plan reduced the [Dmean, Dmax] by [2.09 Gy, 1.19 Gy] for OAR overall, [3.05 Gy, 0.04 Gy] for parotid gland, [3.62 Gy, 5.19 Gy] for larynx, [3.27 Gy, 1.10 Gy] for mandible.

Table 2 reports the Wilcoxon signed rank test of SID-100 and SID-50 for all PTV and OAR statistics. SID-100 and SID-50 are significantly different ($p<0.05$) in PTV homogeneity, PTV maximum dose (D2), R50, Integral dose, OAR max and mean dose. For example, the Wilcoxon signed rank test indicated that the R50 of SID-50 ($M=2.254$; $SD=0.256$) was statistically significantly lower than the R50 of SID-100 ($M=2.381$; $SD=0.236$), $p < 0.05$.

4. Discussion

Recent progress in non-coplanar radiotherapy reveals significant dosimetric improvement from the coplanar IMRT and VMAT (Dong *et al* 2013b, Nguyen *et al* 2014, Lyu *et al* 2018b, Breedveld *et al* 2012, Murzin *et al* 2018, Smyth *et al* 2013, 2016, Chapet *et al* 2006, Laing *et al* 1993, Meedt *et al* 2003). But the clinical translation is hindered by the difficulty of delivering non-coplanar beams on the conventional C-arm platform. CyberKnife, which mounts the linac head on an articulated robotic arm, was expected to improve the dosimetry substantially with extensive usage of the non-coplanar space. However, besides the unclear dosimetric benefit and low treatment delivery efficiency due to the lack of posterior beams and the limitation from its heuristic optimization algorithm (Lin *et al* 2014), CyberKnife is limited in its versatility to treat large tumors. Therefore, the new robotic linac platform currently under development must overcome the following three inter-correlated challenges: 1. A more effective inverse optimization algorithm to create a superior quality treatment plan that can be efficiently delivered. 2. More compact linac head and modified robotic arm to access all 4π steradian angles. 3. The ability to treat large tumors without sacrificing efficiency and modulation resolution. Our previously developed optimization algorithm for 4π IMRT on the C-arm platform paved the foundation to solve the first challenge (O'Connor *et al* 2017). The second challenge can be overcome by the development of a more compact 6MV linac and using flexible distances between the source and the MLC. Here, we describe a solution to the third problem, which is to solve an integrated many-isocenter planning

problem. The term “many-isocenter” is used based on two considerations. First, it provides the necessary differentiation from conventional “multiple-isocenter” treatment planning without integrated isocenter selection, beam orientation, and fluence map optimization. Second, the platform affords a significant increase in the isocenter number. Twelve isocenters were used in one case but more is possible, adding a new degree of freedom to static beam IMRT and non-coplanar modulated arc therapy (Lyu *et al* 2018b) optimization. In the current implementation, the new degree of freedom affords both the large tumor coverage and high intensity modulation resolution. With the same number of beams, the many-isocenter plans significantly improved the dose compactness as indicated by R50, and reduced both OAR and integral doses, thereby achieving overall superior plan quality to the single isocenter plans delivered at twice the distance. The plan efficiency comparison depends on the type of treatment. For regular fractionated radiotherapy, 20-beam SID-50 plans are on average 36% more time-consuming than the SID-100 plans with the same number of beams. For SBRT patients, assuming both plans have the same number of beams, the delivery time of SID-50 and SID-100 plan is comparable, and SID-50 has evident dosimetric advantages. As shown by Figure 3, there is space for further dosimetric improvement by allowing more beams if the dosimetry is prioritized over the delivery efficiency. Therefore, our method offers a solution to a basic conflict between the field-of-view and the intensity modulation resolution in robotic radiotherapy, and to an extent, C-arm gantry radiotherapy. By resolving this conflict, both high MLC resolution and large FOV can be achieved without sacrificing delivery efficiency.

In the past, numerous studies have reported stochastic and heuristic algorithms for BOO in IMRT, such as genetic algorithms (Li *et al* 2004, 2005), simulated annealing (Pugachev and Xing 2002), and column generation (Romeijn *et al* 2005). Among them, the column generation algorithm has been extensively used for recent 4π radiotherapy research (Dong *et al* 2014a, Tran *et al* 2017, Woods *et al* 2018, Murzin *et al* 2018, Woods *et al* 2016). Column generation is a greedy method that iteratively adds new beams to the beam pool based on previously selected beams. A practical limitation is that the runtimes do not scale well with the number of beams to be selected, because it requires solving a larger optimization subproblem as more beams are added to the selected beam pool (O’Connor *et al* 2017). Although coplanar IMRT only requires 7 to 9 beams, it has been shown that use of more beams is desirable for non-coplanar delivery (Dong et al., 2013), and possibly even more should be used for non-coplanar treatment with many isocenters. In this study, we used a group-sparsity regularized beam selection algorithm, which starts with all candidate beams and gradually reduces the number of active beams until the desired number is reached. This non-greedy approach is insensitive to the desired number of beams.

First-order algorithms are well-suited for solving large-scaled optimization problem. The primal-dual hybrid gradient (PDHG) algorithm (Chambolle and Pock 2011) is one first-order method that has been investigated in our previous studies on FMO (Nguyen *et al* 2015, 2016, 2017). The PDHG algorithm has been compared favorably to the alternating direction method of multipliers (ADMM) (Boyd 2011) due to its reduced computation cost within each iteration. The former only needs matrix multiplication, and the latter requires solving a linear system of equation involving the large dose contribution matrix. In this study, the optimization problem (1) was solved using FISTA (Beck and Teboulle 2009), which not only

has simple iterations but also achieves a convergence rate of $O\left(\frac{1}{k^2}\right)$, substantially faster than the $O\left(\frac{1}{k}\right)$ convergence rate of ADMM and PDHG. Subsequently, FISTA is well-suited for large-scaled treatment planning problems with a large number of candidate beams, such as in beam angle selection (O'Connor *et al* 2018, 2017) and VMAT optimization (Lyu *et al* 2019, 2018a). The most computationally expensive step in FISTA is the matrix multiplication. Further acceleration of the optimization can be achieved by using graphic processing units (GPUs) for parallel computing (Owens *et al* 2008).

Due to the computation challenge of dose calculation/optimization of the vast combination of all possible beams, this study is restricted to SID of 50cm and 100cm, and the number of isocenter candidates is heuristically determined. In a more general many-isocenter optimization scenario, both SID and location of the isocenters could be optimized for greater dosimetric and delivery efficiency versatility. New mathematical paradigms may be needed to solve the optimization problem that is orders of magnitude larger.

5. Conclusion

This study investigates the feasibility of 4π radiotherapy using many isocenters on a robotic platform to treat large targets with high intensity modulation resolution. Without sacrificing delivery efficiency, the many-isocenter plans delivered at shorter SID significantly improved dose compactness and OAR sparing compared with large FOV plans delivered at a longer SID.

Supplementary Material

Refer to Web version on PubMed Central for supplementary material.

Acknowledgment

This research is supported by DOE Grants Nos. DE-SC0017057 and DE-SC0017687, NIH Grants Nos. R01CA188300, R01CA230278, R21CA228160 and R44CA183390.

Appendix A1: The Fast Iterative Shrinkage-Thresholding Algorithm (FISTA)

FISTA solves an optimization problem that can be formulated as

$$\text{minimize } F(x) + G(x),$$

where F is a differentiable convex function with a Lipschitz continuous gradient, and G is a convex function which has a proximal operator that can be evaluated efficiently (Beck & Teboulle 2009). Algorithm 3 presents the pseudocode of FISTA with line search algorithm, where the key steps are the evaluation of the gradient of F and the proximal operator of G. The proximal operator (Parikh and Boyd 2013) of a function G with step size t is defined by

$$\text{Prox}_{tG}(x) = \underset{Z}{\text{argmin}}\left(G(z) + \frac{1}{2t}\|z - x\|_2^2\right).$$

To facilitate the application of FISTA, we replaced the l_1 norm in the TV regularization term by the Huber penalty (Noe 1930) defined as

$$H(x) = \|x\|_1(\mu) = \sum_i |x_i|^{(\mu)}, \quad \text{where } |x_i|^{(\mu)} = \begin{cases} \frac{1}{2\mu}x_i^2, & |x_i| \le \mu \\ |x_i| - \frac{\mu}{2}, & |x_i| > \mu \end{cases}.$$

The Huber penalty provides a convex, differentiable approximation to the l_1 norm, with a $\frac{1}{\mu}$ –Lipschitz continuous gradient.

To apply FISTA on the BOO problem, the objective function in Equation (1) is written in the canonical FISTA form by defining F and G as

$$F(x) = \frac{1}{2}\|W(Ax - d)\|_2^2 + \lambda \|Dx\|_1^{(\mu)}$$

$$G(x) = \sum_{b,i} w_{b,i} \|x_{b,i}\|_2^{\frac{1}{2}} + I_+(x), \quad \text{where } I_+(x) = \begin{cases} 0 & if\ x \ge 0 \\ \infty & \text{otherwise} \end{cases},$$

The gradient of F can be evaluated efficiently through the chain rule

$$\nabla F(x) = A^T W^2 (Ax - d) + \frac{\lambda}{\mu} D^T P_{[-\mu, \mu]}(Dx),$$

where $P_{[-\mu,\mu]}$ is the projection onto the hypercube $\{x | -\mu \le x_i \le \mu, \forall i\}$. The proximal operator of G is

$$(\text{Prox}_{tG}(x))_{b,i} = \text{Prox}_{tw_{b,i}\|\cdot\|_2^{1/2}}(\max(x_{b,i}, 0))$$

The proximal operator of $h(x) = \|x\|_2^{\frac{1}{2}}$ has an explicit solution (Möllenhoff *et al* 2015). Let $\alpha = t/\|y\|_2^{3/2}$, then

$$\text{Prox}_{th}(y) = s^2 y, \quad \text{where } \begin{cases} \frac{2}{\sqrt{3}} \sin\left(\frac{1}{3}\arccos\left(\frac{3\sqrt{3}}{4}\alpha\right) + \frac{\pi}{2}\right) & \text{if } \alpha \le \frac{2\sqrt{6}}{9} \\ 0 & \text{otherwise} \end{cases}$$

Pseudocode for FISTA with line search

Initialize $x_0 := 0, v_0 := x_0, t_0 > 0, r_1 > 1, r_2 > 1$

for $k = 1, 2, \ldots$ *do*

  $t := r_1 t_{k-1}$

  Repeat

    $\theta := \begin{cases} 1 & \text{if } k = 1 \\ \text{positive root of } t_{k-1}\theta^2 = t\theta_{k-1}^2(1-\theta) & \text{if } k > 1 \end{cases}$

    $y := (1-\theta)x_{k-1} + \theta v_{k-1}$

    $x := \text{Prox}_{tG}(y - t\nabla F(y))$

    break if $F(x) \le F(y) + < \nabla F(y), x - y > + \frac{1}{2t}\|x - y\|_2^2$

    $t := t/r_2$

  $t_k := t$

  $\theta_k := \theta$

  $v_k := x_k + \frac{1}{\theta_k}(x - x_k)$

  break if $\frac{\|x - x_k\|}{\|x_k\|} \le \epsilon$

  $x_k := x$

end for

return x

Algorithm 3: FISTA with line search

REFERENCES

Amoush A, Murray E, Yu JS and Xia P 2015 Single-isocenter hybrid IMRT plans versus two-isocenter conventional plans and impact of intrafraction motion for the treatment of breast cancer with supraclavicular lymph nodes involvement J. Appl. Clin. Med. Phys

Beck A and Teboulle M 2009 A Fast Iterative Shrinkage-Thresholding Algorithm Soc. Ind. Appl. Math. J. Imaging Sci 2 183–202

Blumensath T and Davies ME 2010 Normalized iterative hard thresholding: Guaranteed stability and performance IEEE J. Sel. Top. Signal Process

Boyd S 2011 Alternating Direction Method of Multipliers Proc. 51st IEEE Conf. Decis. Control 3 1–44 Online: http://www.nowpublishers.com/product.aspx?product=MAL&doi=2200000016

Brahme A, Roos JE and Lax I 1982 Solution of an integral equation encountered in rotation therapy *Phys*. Med. Biol

Breedveld S, Storchi PRM, Voet PWJ and Heijmen BJM 2012 ICycle: Integrated, multicriterial beam angle, and profile optimization for generation of coplanar and noncoplanar IMRT plans Med. Phys

Chambolle A and Pock T 2011 A first-order primal-dual algorithm for convex problems with applications to imaging J. Math. Imaging Vis 40 120–45

Chapet O, Khodri M, Jalade P, N'guyen D, Flandin I, D'hombres A, Romestaing P and Mornex F 2006 Potential benefits of using non coplanar field and intensity modulated radiation therapy to preserve the heart in irradiation of lung tumors in the middle and lower lobes Radiother. Oncol

Dong P, Lee P, Ruan D, Long T, Romeijn E, Low DA, Kupelian P, Abraham J, Yang Y and Sheng K 2013a 4π Noncoplanar Stereotactic Body Radiation Therapy for Centrally Located or Larger Lung Tumors Int. J. Radiat. Oncol 86 407–13 Online: http://linkinghub.elsevier.com/retrieve/pii/S0360301613001636

Dong P, Lee P, Ruan D, Long T, Romeijn E, Yang Y, Low D, Kupelian P and Sheng K 2013b 4π non-coplanar liver SBRT: A novel delivery technique Int. J. Radiat. Oncol. Biol. Phys

Dong P, Nguyen D, Ruan D, King C, Long T, Romeijn E, Low DA, Kupelian P, Steinberg M, Yang Y and Sheng K 2014a Feasibility of prostate robotic radiation therapy on conventional C-arm linacs Pract. Radiat. Oncol

Dong P, Yu V, Nguyen D, Demarco J, Woods K, Boucher S, Low DA and Sheng K 2014b Feasibility of using intermediate x-ray energies for highly conformal extracranial radiotherapy Med. Phys

Ee236C 2013 Fast proximal gradient methods 1–32

Grégoire V and Mackie TR 2011 State of the art on dose prescription, reporting and recording in Intensity-Modulated Radiation Therapy (ICRU report No. 83) Cancer/Radiotherapie 15 555–9

Hong L, Alektiar K, Chui C, LoSasso T, Hunt M, Spirou S, Yang J, Amols H, Ling C, Fuks Z and Leibel S 2002 IMRT of large fields: Whole-abdomen irradiation Int. J. Radiat. Oncol. Biol. Phys

Kim MM, Kennedy C, Scheuermann R, Freedman G and Li T 2019 Whole Breast and Lymph Node Irradiation using Halcyon™ 2.0 Utilizing Automatic Multi-isocenter Treatment Delivery and Daily Kilovoltage Cone-beam Computed Tomography Cureus

Krayenbuehl J, Davis JB and Ciernik IF 2006 Dynamic intensity-modulated non-coplanar arc radiotherapy (INCA) for head and neck cancer Radiother. Oncol 81 151–7 [PubMed: 17055095]

Laing R, Bentley R, Nahum A and Brada M 1993 Stereotactic radiotherapy for irregular targets: Comparison between non-coplanar arcs and static non-coplanar conformal beams Eur. J. Cancer

Li Y, Yao D, Yao J and Chen W 2005 A particle swarm optimization algorithm for beam angle selection in intensity-modulated radiotherapy planning. Phys. Med. Biol 50 3491–514 [PubMed: 16030379]

Li Y, Yao J and Yao D 2004 Automatic beam angle selection in IMRT planning using genetic algorithm Phys Med Biol 49 1915–32 [PubMed: 15214533]

Lin YW, Lin KH, Ho HW, Lin HM, Lin LC, Lee SP and Chui CS 2014 Treatment plan comparison between stereotactic body radiation therapy techniques for prostate cancer: Non-isocentric CyberKnife versus isocentric RapidArc Phys. Medica

Lyu Q, Neph R, Yu VY, Ruan D and Sheng K 2019 Single-arc VMAT optimization for duallayer MLC Phys. Med. Biol

Lyu Q, O'Connor D, Ruan D, Yu V, Nguyen D and Sheng K 2018a VMAT optimization with dynamic collimator rotation Med. Phys 45

Lyu Q, Yu VY, Ruan D, Neph R, O'Connor D and Sheng K 2018b A novel optimization framework for VMAT with dynamic gantry couch rotation Phys. Med. Biol 63

Meedt G, Alber M and Nüsslin F 2003 Non-coplanar beam direction optimization for intensity-modulated radiotherapy Phys. Med. Biol

Möllenhoff T, Strekalovskiy E, Moeller M and Cremers D 2015 Low Rank Priors for Color Image Regularization

Murzin VL, Woods K, Moiseenko V, Karunamuni R, Tringale KR, Seibert TM, Connor MJ, Simpson DR, Sheng K and Hattangadi-Gluth JA 2018 4π plan optimization for cortical-sparing brain radiotherapy Radiother. Oncol

Neph R, Ouyang C, Neylon J, Yang Y and Sheng K 2019 Parallel beamlet dose calculation via beamlet contexts in a distributed multi-GPU framework Med. Phys 0 Online: 10.1002/mp.13651

Nguyen D, Lyu Q, Ruan D, O'Connor D, Low DA and Sheng K 2016 A comprehensive formulation for volumetric modulated arc therapy planning Med. Phys 43

Nguyen D, O'Connor D, Ruan D and Sheng K 2017 Deterministic direct aperture optimization using multiphase piecewise constant segmentation Med. Phys

Nguyen D, O'Connor D, Yu VY, Ruan D, Cao M, Low D a. and Sheng K 2015 Dose domain regularization of MLC leaf patterns for highly complex IMRT plans. Med. Phys 42 1858–70 Online: http://scitation.aip.org/content/aapm/journal/medphys/42/4/10.1118/1.4915286%5Cnhttp://www.ncbi.nlm.nih.gov/pubmed/25832076 [PubMed: 25832076]

Nguyen D, Rwigema J-C M, Yu VY, Kaprealian T, Kupelian P, Selch M, Lee P, Low D a K 2014 Feasibility of extreme dose escalation for glioblastoma multiforme using 4pi radiotherapy. Radiat. Oncol 9 239 Online: http://www.pubmedcentral.nih.gov/articlerender.fcgi?artid=4230756&tool=pmcentrez&rendertype=abstract [PubMed: 25377756]

Noe M 1930 The Annals of Mathematical Statistics Ann. Math. Stat 1 1–2

O'Connor D, Voronenko Y, Nguyen D, Yin W and Sheng K 2017 Fast non-coplanar beam orientation optimization based on group sparsity Online: https://arxiv.org/abs/1710.05308

O'Connor D, Yu V, Nguyen D, Ruan D and Sheng K 2018 Fraction-variant beam orientation optimization for non-coplanar IMRT Phys. Med. Biol

Owens JD, Houston M, Luebke D, Green S, Stone JE and Phillips JC 2008 GPU computing Proc. IEEE

Parikh N and Boyd S 2013 Proximal Algorithms Found. Trends Optim 1 123–231

Pollom E, Wang L, Gibbs IC and Soltys SG 2019 CyberKnife Robotic Stereotactic Radiosurgery BT - Stereotactic Radiosurgery and Stereotactic Body Radiation Therapy: A Comprehensive Guide ed Trifiletti DM, Chao ST, Sahgal A and Sheehan JP (Cham: Springer International Publishing) pp 67–76 Online: 10.1007/978-3-030-16924-4_6

Pugachev A, Li JG, Boyer AL, Hancock SL, Le QT, Donaldson SS and Xing L 2001 Role of beam orientation optimization in intensity-modulated radiation therapy Int. J. Radiat. Oncol. Biol. Phys 50 551–60 [PubMed: 11380245]

Pugachev A and Xing L 2002 Incorporating prior knowledge into beam orientaton optimization in IMRT Int. J. Radiat. Oncol. Biol. Phys

Rao M, Yang W, Chen F, Sheng K, Ye J, Mehta V, Shepard D and Cao D 2010 Comparison of Elekta VMAT with helical tomotherapy and fixed field IMRT: plan quality, delivery efficiency and accuracy. Med. Phys 37 1350–9 [PubMed: 20384272]

Reinelt G. 1991TSPLIB—A Traveling Salesman Problem Library. ORSA J. Comput.

Romeijn HE, Ahuja RK, Dempsey JF and Kumar A 2005 A Column Generation Approach to Radiation Therapy Treatment Planning Using Aperture Modulation SIAM J. Optim

Smyth G, Bamber JC, Evans PM and Bedford JL 2013 Trajectory optimization for dynamic couch rotation during volumetric modulated arc radiotherapy Phys. Med. Biol 58 8163–77 Online: http://stacks.iop.org/0031-9155/58/i=22/a=8163?key=crossref.bc2995836dfb531b0d4154da1bd70c05 [PubMed: 24200876]

Smyth G, Evans PM, Bamber JC and Bedford JL 2019a Recent developments in non-coplanar radiotherapy Br. J. Radiol 92 20180908 Online: https://www.birpublications.org/doi/10.1259/bjr.20180908 [PubMed: 30694086]

Smyth G, Evans PM, Bamber JC, Mandeville HC, Rollo Moore A, Welsh LC, Saran FH and Bedford JL 2019b Dosimetric accuracy of dynamic couch rotation during volumetric modulated arc therapy (DCR-VMAT) for primary brain tumours Phys. Med. Biol

Smyth G, Evans PM, Bamber JC, Mandeville HC, Welsh LC, Saran FH and Bedford JL 2016 Non-coplanar trajectories to improve organ at risk sparing in volumetric modulated arc therapy for primary brain tumors Radiother. Oncol 121 124–31 [PubMed: 27481571]

Teoh M, Clark CH, Wood K, Whitaker S and Nisbet A 2011 Volumetric modulated arc therapy: A review of current literature and clinical use in practice Br. J. Radiol

Tran A, Zhang J, Woods K, Yu V, Nguyen D, Gustafson G, Rosen L and Sheng K 2017 Treatment planning comparison of IMPT, VMAT and 4Π radiotherapy for prostate cases Radiat. Oncol 12

Vanetti E, Clivio A, Nicolini G, Fogliata A, Ghosh-Laskar S, Agarwal JP, Upreti RR, Budrukkar A, Murthy V, Deshpande DD, Shrivastava SK, Dinshaw KA and Cozzi L 2009 Volumetric modulated arc radiotherapy for carcinomas of the oro-pharynx, hypo-pharynx and larynx: A treatment planning comparison with fixed field IMRT Radiother. Oncol

Voet PWJ, Breedveld S, Dirkx MLP, Levendag PC and Heijmen BJM 2012 Integrated multicriterial optimization of beam angles and intensity profiles for coplanar and noncoplanar head and neck IMRT and implications for VMAT Med. Phys

Wang Z, Jiang W, Feng Y, Guo Y, Cong Z, Song B and Guo Y 2013 A simple approach of three-isocenter IMRT planning for craniospinal irradiation Radiat. Oncol

Wilson B, Otto K and Gete E 2017 A simple and robust trajectory-based stereotactic radiosurgery treatment: Med. Phys

Woods K, Lee P, Kaprealian T, Yang I and Sheng K 2018 Cochlea-sparing acoustic neuroma treatment with 4π radiation therapy Adv. Radiat. Oncol

Woods K, Nguyen D, Tran A, Yu VY, Cao M, Niu T, Lee P and Sheng K 2016 Viability of Noncoplanar VMAT for liver SBRT compared with coplanar VMAT and beam orientation optimized 4π IMRT Adv. Radiat. Oncol 1 67–75 [PubMed: 27104216]

Xia P and Verhey LJ 1998 Multileaf collimator leaf sequencing algorithm for intensity modulated beams with multiple static segments Med. Phys

Yang J, Fowler JF, Lamond JP, Lanciano R, Feng J and Brady LW 2010 Red Shell: Defining a High-Risk Zone of Normal Tissue Damage in Stereotactic Body Radiation Therapy Int. J. Radiat. Oncol. Biol. Phys

Yu VY, Landers A, Woods K, Nguyen D, Cao M, Du D, Chin RK, Sheng K and Kaprealian TB 2018 A Prospective 4π Radiation Therapy Clinical Study in Recurrent High-Grade Glioma Patients Int. J. Radiat. Oncol. Biol. Phys

Yu VY, Tran A, Nguyen D, Cao M, Ruan D, Low DA and Sheng K 2015 The development and verification of a highly accurate collision prediction model for automated noncoplanar plan delivery Med. Phys 42 6457–67 Online: http://www.ncbi.nlm.nih.gov/pmc/articles/PMC4608969/ [PubMed: 26520735]

Zeng GG, Heaton RK, Catton CN, Chung PW, O'Sullivan B, Lau M, Parent A and Jaffray DA 2007 A two isocenter IMRT technique with a controlled junction dose for long volume targets Phys. Med. Biol

Zhu L, Lee L, Ma Y, Ye Y, Mazzeo R and Xing L 2008 Using total-variation regularization for intensity modulated radiation therapy inverse planning with field-specific numbers of segments Phys. Med. Biol 53 6653–72 Online: http://stacks.iop.org/0031-9155/53/i=23/a=002?key=crossref.0031cfaebafb43bc3cf895696db4929d [PubMed: 18997262]

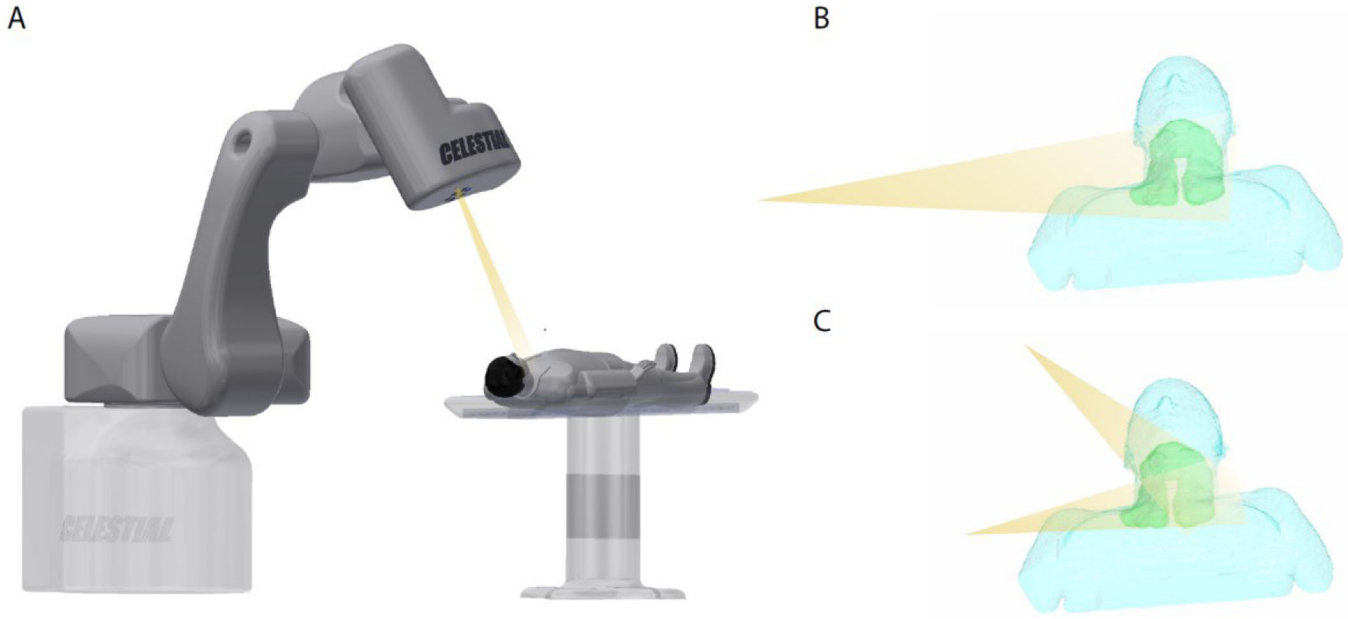

Figure 1.

(A) Demonstration of the robotic arm platform, (B) an isocentric SID-100 beam that covers the entire target, (C) beams of different isocenters are required to efficiently cover the entire target.

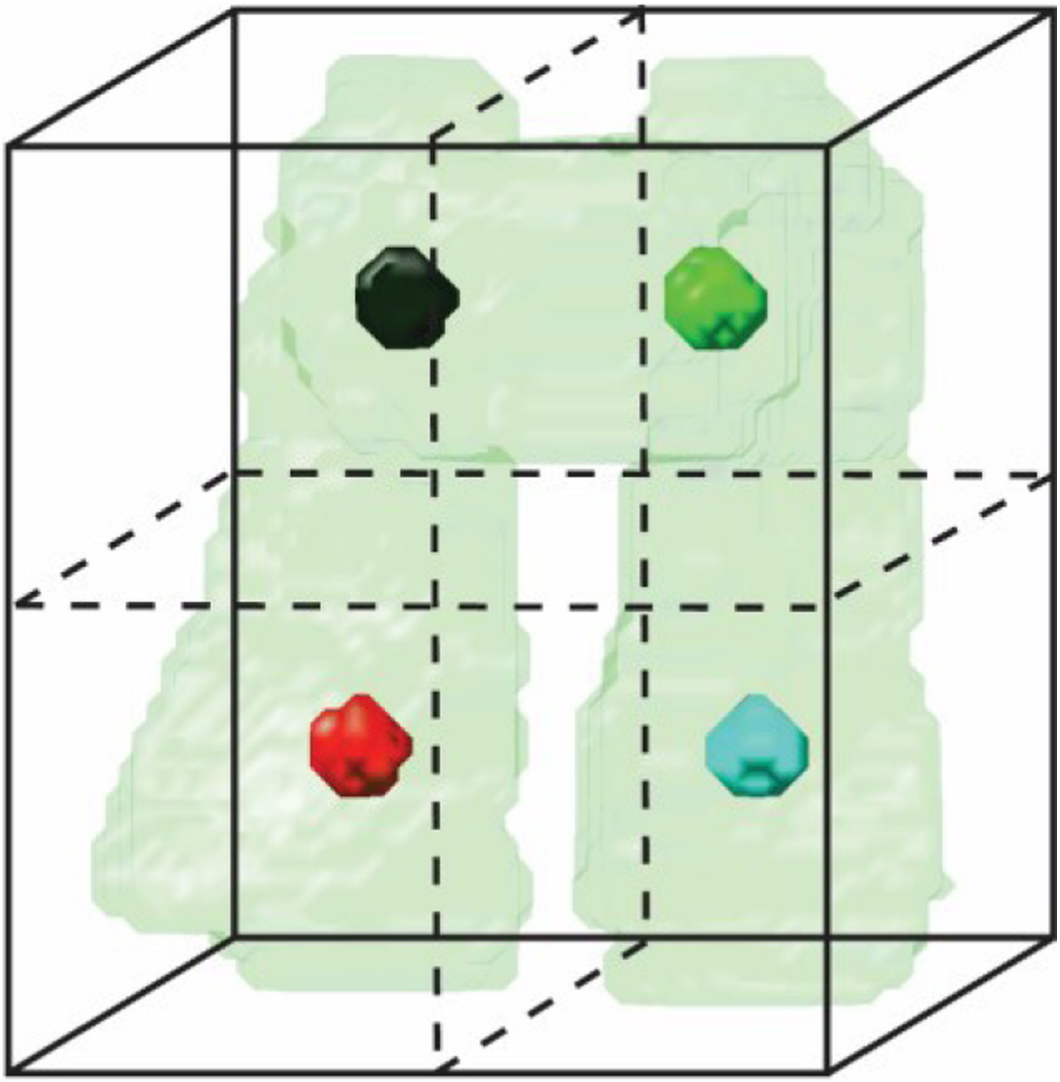

Figure 2.
Illustration of the PTV, bounding box, and four isocenters.

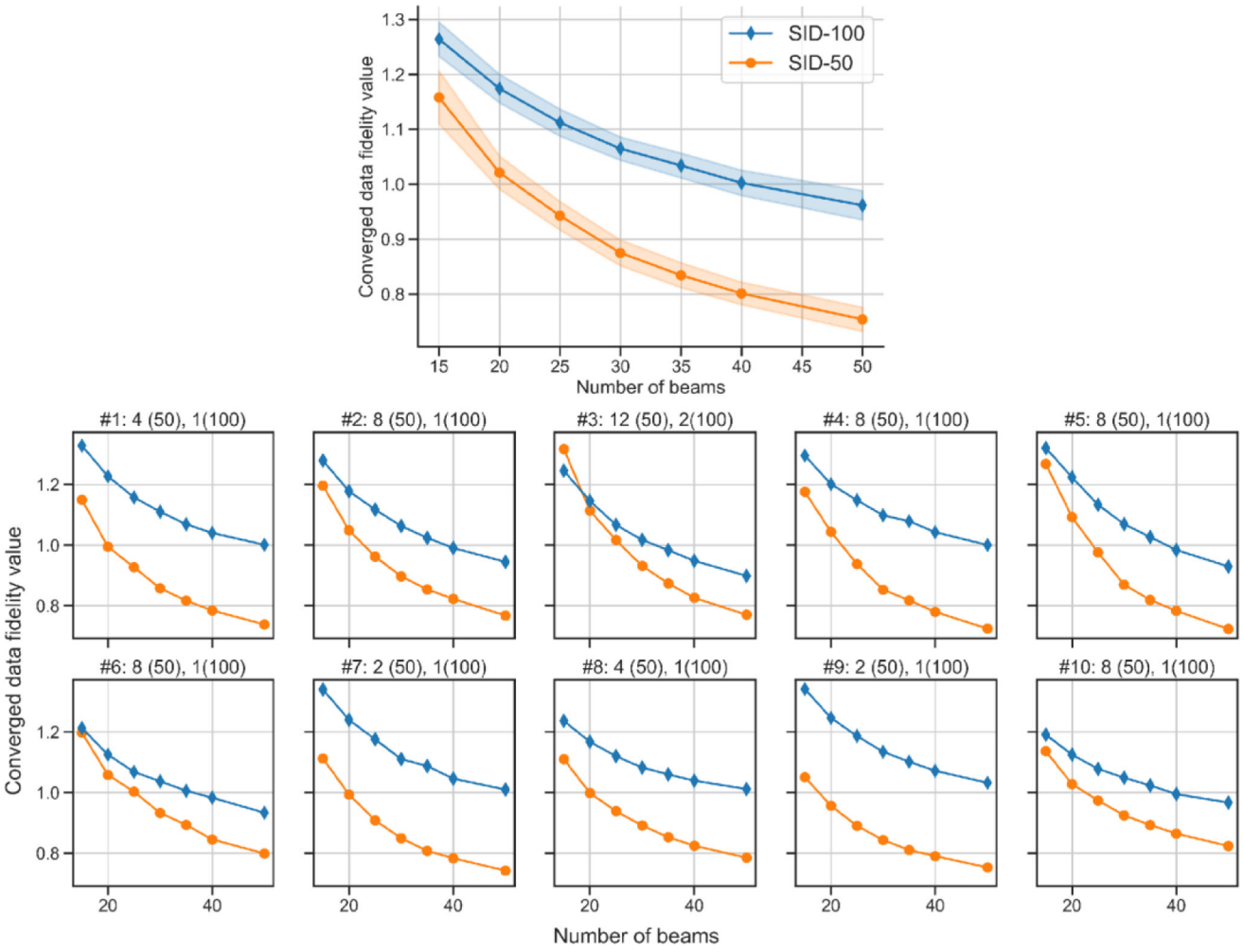

Figure 3.

Final data fidelity value vs the number of beams. The plot with shaded error bar shows a summary of all patients. Each patient plot is titled with the patient number, the number of isocenters for the SID-50 plan, and the number of isocenters for the SID-100 plan. For example, the first patient plot is entitled: '#1: 4(50), 1(100)', showing that the patient #1 has four isocenters for the SID-50 plan, and one isocenter for the SID-100 plan.

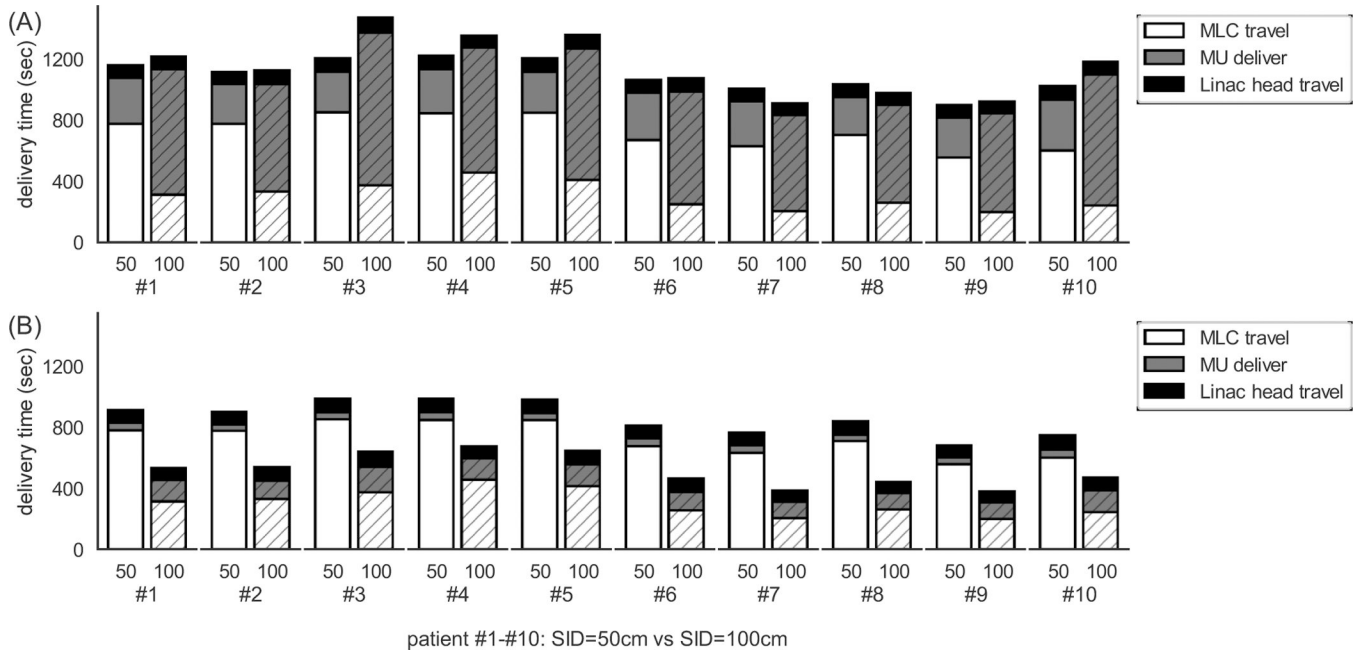

Figure 4.
Delivery time estimation assuming (A) 5 fractions and (B) 30 fractions for all 20-beam plans.

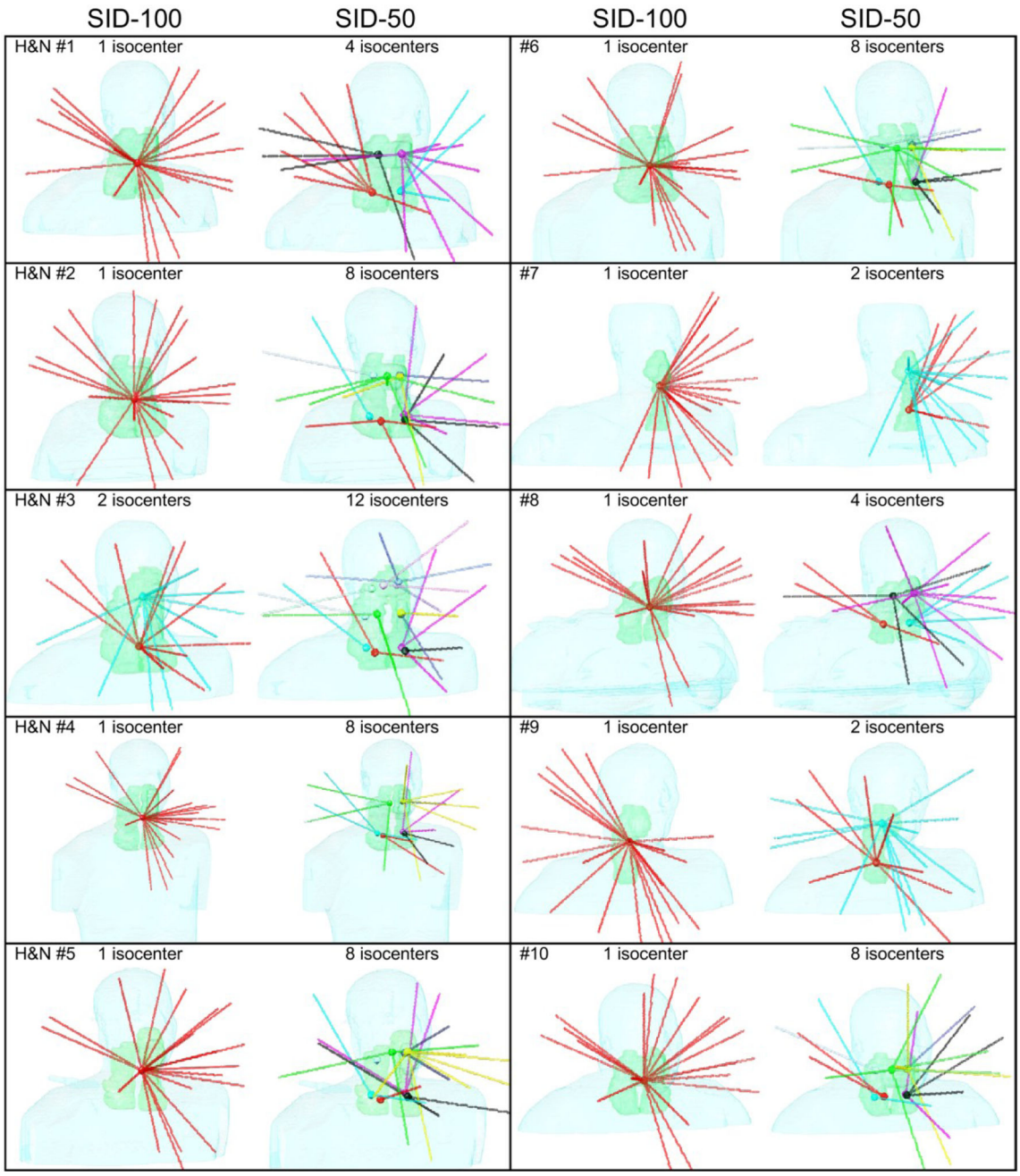

Figure 5.
Selected beams in the 20-beam plans of all patients

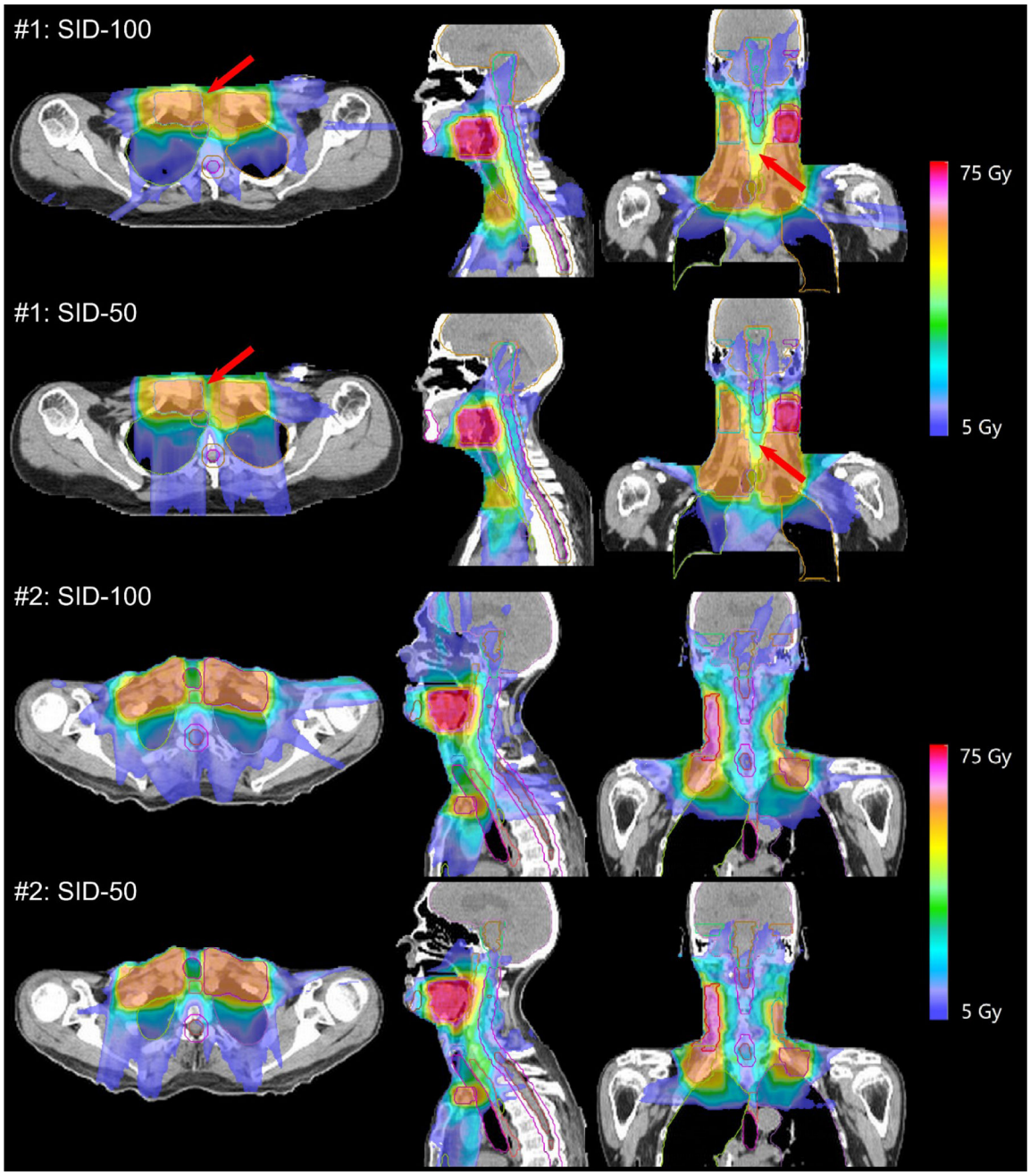

Figure 6.
Isodose colorwash of 20-beam SID-100 and SID-50 plans for two patients (#1 and #2, having 4 and 8 isocenters in the SID-50 plan respectively).

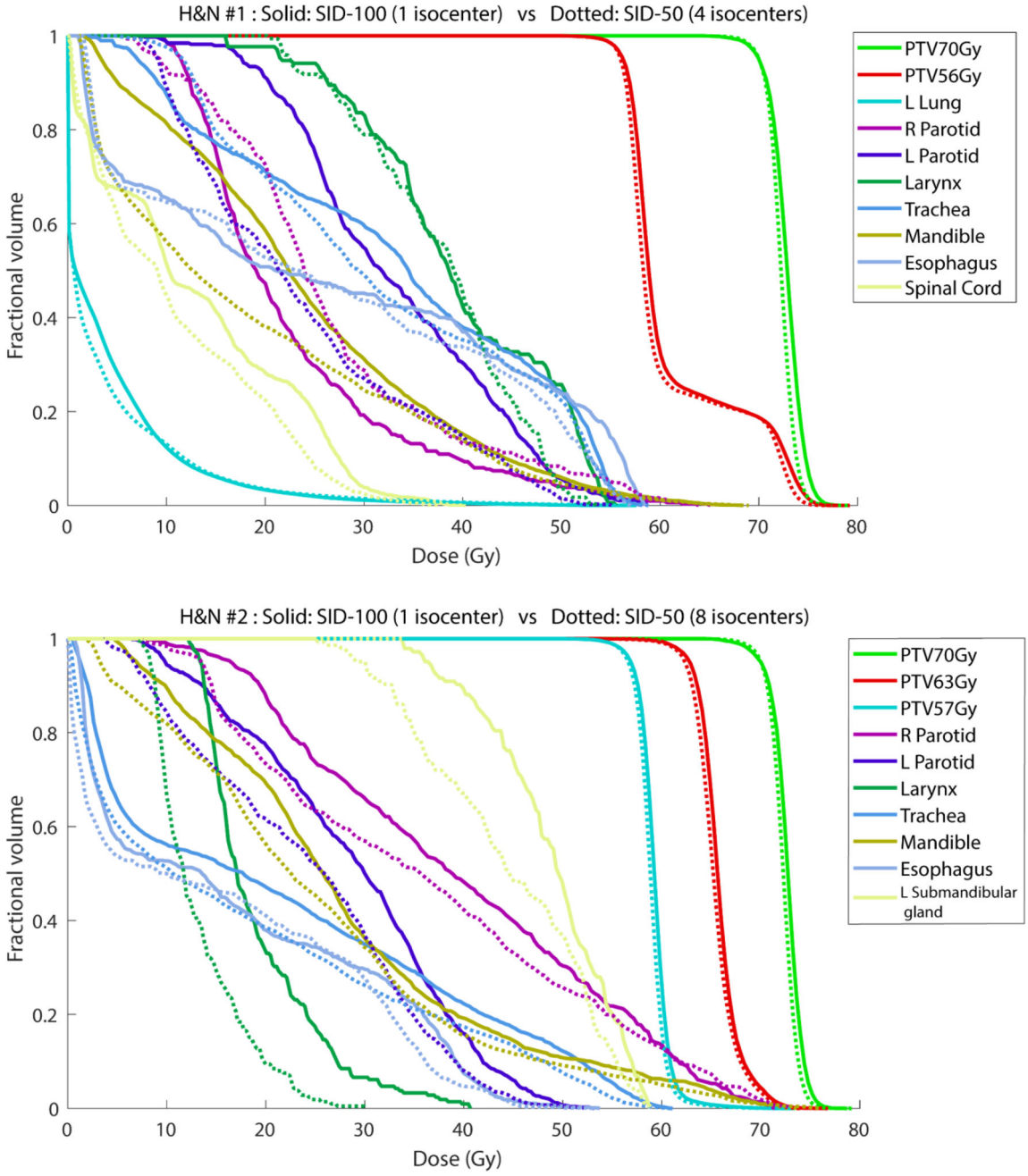

Figure 7.

DVH comparison of the 20-beam plans using SID-100 (solid) and SID-50 (dotted) for selected two patients (#1 and #2, having 4 and 8 isocenters in the SID-50 plan respectively). D95 of the PTV with highest prescription dose is normalized to the prescription dose.

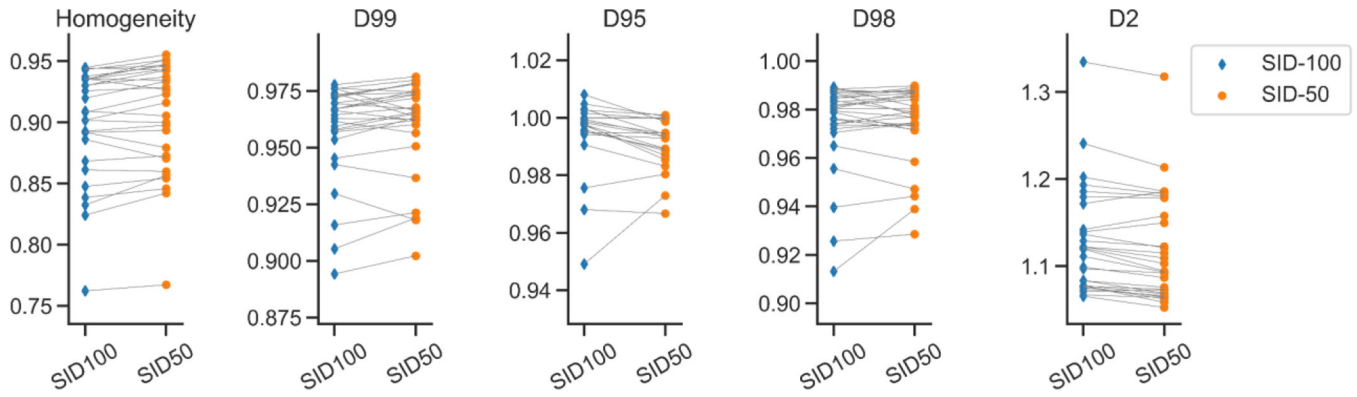

Figure 8.

PTV statistics comparison of the 20-beam SID-100 (blue) and SID-50 (orange), for all PTVs (29 PTVs in total). The same PTV of the two plans are connected with lines. D2, D95, D98, and D99 are normalized by the prescription dose.

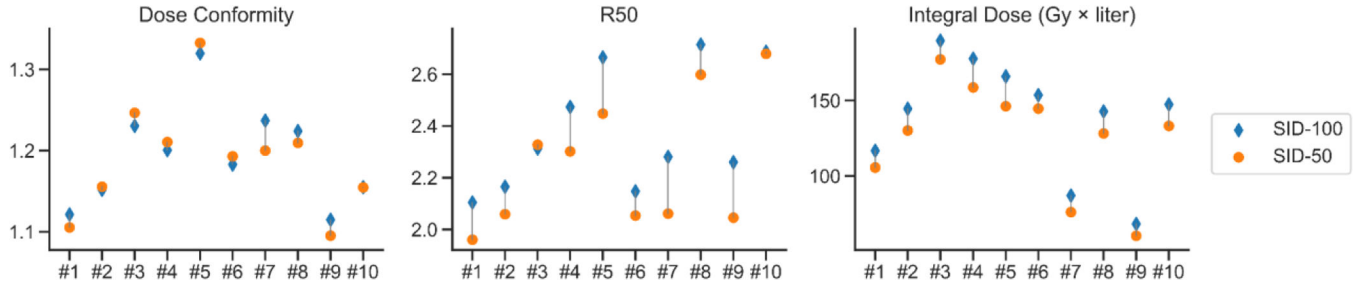

Figure 9.

Dose conformity, R50, and integral dose for all patients (#1-#10). All plans have 20 beams in total. The SID-100 plan (blue) and the SID-50 plan (orange) of the same patient are connected with lines.

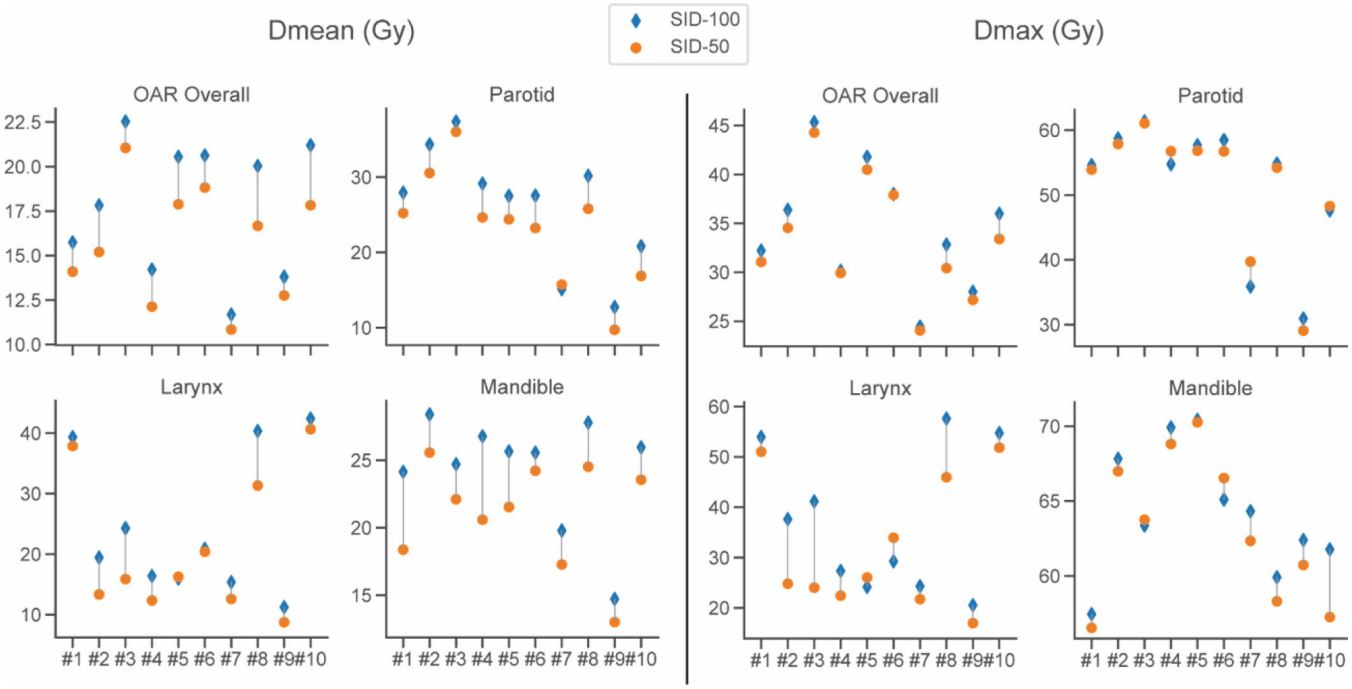

Figure 10.

Mean and maximum dose for OAR overall and selected critical OARs including parotid gland, larynx, and mandible, for all patients (#1-#10). All plans have 20 beams in total. The SID-100 plan (blue) and the SID-50 plan (orange) of the same patient are connected with lines.

Table 1

PTV volumes, PTV bounding box dimensions, number of isocenters, number of sampled beams, and number of candidate beams (non-colliding beams) for all patients.

Patient	PTV volume (cm^3)	Bounding Box (cm)			Isocenter #		Sampled beam #		Candidate beam #	
		x	y	z	SID-100	SID-50	SID-100	SID-50	SID-100	SID-50
H&N#1	610.5	9.3	14.3	15.8	1	4	1162	4648	776	2785
H&N#2	724.6	10.8	16.0	18.3	1	8	1162	2320	826	1440
H&N#3	947.0	10.0	17.0	22.3	2	12	2324	3480	1579	2117
H&N#4	785.0	10.3	15.5	19.0	1	8	1162	2320	891	1452
H&N#5	686.4	10.5	14.5	18.3	1	8	1162	2320	824	1422
H&N#6	787.0	10.5	16.5	17.5	1	8	1162	2320	842	1443
H&N#7	352.7	8.5	8.5	18.5	1	2	1162	2324	758	1315
H&N#8	555.7	9.8	13.3	14.8	1	4	1162	4648	906	2904
H&N#9	271.3	8.8	6.8	17.0	1	2	1162	2324	781	1385
H&N#10	620.5	10.3	15.0	14.0	1	8	1162	2320	685	1278

Table 2

Wilcoxon signed rank test of SID-100 and SID-50 for the PTV and OAR statistics in the 20-beam plans.

Statistics	P-value	Signed rank	Number of samples	SID-100		SID-50		(SID-50)-(SID-100)	
				Mean	STD	Mean	STD	Mean	STD
PTV Homogeneity	0.003	85	29	0.901	0.045	0.906	0.045	0.005	0.009
PTV D99	0.062	131	29	0.958	0.022	0.96	0.021	0.002	0.006
PTV D98	0.749	202	29	0.974	0.019	0.975	0.016	0.001	0.007
PTVD2	<.001	380	29	1.127	0.062	1.118	0.061	−0.009	0.01
Dose Conformity	0.625	33	10	1.194	0.062	1.19	0.069	−0.003	0.017
R50	0.006	53	10	2.381	0.236	2.254	0.256	−0.127	0.083
Integral Dose	0.002	55	10	139.377	38.481	126.02	36.139	−13.357	3.911
OAR Dmean	0.002	55	10	17.822	3.727	15.729	3.273	−2.094	0.894
OAR Dmax	0.002	55	10	34.515	6.317	33.325	6.173	−1.19	0.874